



Three dimensional few-layer porous carbon nanosheets towards oxygen reduction

Jian Zhang^{a,1}, Chenyu Zhang^{a,1}, Yufeng Zhao^{b,*}, Ibrahim Saana Amiinu^a, Huang Zhou^a, Xiaobo Liu^a, Yongfu Tang^b, Shichun Mu^{a,*}

^a State Key Laboratory of Advanced Technology for Materials Synthesis and Processing, Wuhan University of Technology, Wuhan 430070, China

^b Key Laboratory of Applied Chemistry, Yanshan University, Qinhuangdao 066004, China

ARTICLE INFO

Article history:

Received 15 December 2016

Received in revised form 4 March 2017

Accepted 12 April 2017

Available online 14 April 2017

Keywords:

Carbon nanosheet

Nitrogen doping

Biomass

Cellulose

Oxygen reduction

ABSTRACT

Novel three dimensional (3D) porous carbon nanosheets with few layers are successfully prepared using intrinsically porous cellulose as carbon matrix only by means of calcination and KOH activation. Further, the N-doped 3D carbon nanosheets show high density of pyridinic N and extremely high specific surface area ($1756 \text{ m}^2 \text{ g}^{-1}$). As oxygen reduction catalyst, they possess an outperformed onset ($E_0 = -0.03 \text{ V}$) and half-wave ($E_{1/2} = -0.17 \text{ V}$) potential compared with the platinum (Pt) electrocatalyst ($E_0 = -0.05 \text{ V}$, $E_{1/2} = -0.2 \text{ V}$) in an alkaline system. In addition, excellent electrochemical stability as well as improved CO poisoning resistance and suppressed methanol crossover relative to Pt is also obtained. In an acid system, the catalyst also exhibits good activity and higher durability than Pt/C. Significantly, when used as a catalyst of the air electrode for Zn–air batteries, it demonstrates a higher peak power density of 208 mW cm^{-2} and a voltage plateau at the controlled discharge current density compared to the commercial Pt/C electrode. This simple and scalable approach provides a direct route to synthesize low cost and highly efficient electrocatalysts from biomass without addition of extra metal catalysts.

© 2017 Elsevier B.V. All rights reserved.

1. Introduction

Low temperature fuel cells (LTFC) have drew widespread consideration owing to their low temperature of operation, environmental friendliness, and high energy conversion efficiency [1]. The main challenge in their commercialization is the development of low cost and highly efficient electrocatalysts to overcome the stagnant oxygen reduction reaction (ORR) occurring at the cathode [2,3]. Hitherto, Pt or Pt-based metal-alloys are known to be the best efficient catalysts for ORR [4]. However, commercial-scale implementation is heavily restricted due to their colossal cost and scarceness. Moreover, Pt-based catalysts also endure poor durability and CO deactivation [5]. Therefore, extensive efforts have been dedicated to probing highly active and cost-effective metal-free catalysts materials.

Heteroatom-doped carbon-based catalysts have been of concern as extraordinary candidate for ORR considering their worldwide accessibility, corrosion resistance, and environmental

affability [6–9]. N-doped carbon materials, such as mesoporous graphitic arrays, graphene, carbon nanotubes, and fullerenes, have exhibited very good catalytic activity towards ORR [9–13]. For example, N-doped 3D graphene with high specific surface area, abundance pore structures, high electrical conductivity, good chemical stability can be extensively used in energy storage and conversion devices [14,15]. However, the current synthesis approach to obtaining 3D carbon nanomaterials (including pyrolysis of organogels, direct self-assembly of nanocarbon moieties, and chemical vapor deposition, etc.) unavoidably involves the downside such as the use of costly toxic precursors, complicated equipment requirements, and unsatisfied production yields. The practical application demands a cost-effective, facile, and green approach to the large scale fabrication of such 3D nanocarbon frameworks.

Recently, plenty of researchers are focusing on biomass as precursor for the fabrication of high-performance 3D carbon-based frameworks which are cheap, non-toxic and readily available in a large scale [16–19]. As reported, banana peels as a kind of non-recyclable waste, are generated to the tune of 30 million tons worldwide per year without any commercial end use [20]. The banana peel mainly consists of cellulose, which contains highly porous structures and abundant crude proteins (Fig. S1). The use of

* Corresponding authors.

E-mail addresses: yufengzhao@ysu.edu.cn (Y. Zhao), msc@whut.edu.cn, mushichun@gmail.com (S. Mu).

¹ The first two authors contributed equally in this work.

biomass with cellulose as natural precursor could enable the fabrication of 3D carbon nano-frameworks [21,22]. This is the primary motivation for this work.

Herein, we report a novel cost effective, facile, and readily scalable method for the preparation of N-doped 3D structured carbon nanosheets with outstanding electrocatalytic performance from cellulose in biomass. During the synthesis process, besides the intrinsically porous structure, the KOH activation plays an important part in constructing this unique 3D structure. To increase the N content with electrocatalytic activity and further boost the ORR activity, ammonia (NH_3) is introduced during the second heat treatment step. The as-obtained 3D porous carbon sheets demonstrates a very high specific surface area ($1756 \text{ cm}^2 \text{ g}^{-1}$) and contains numerous mesopores that can produce potential abundance catalytic sites. These are beneficial for outperforming the commercial Pt/C catalyst in ORR activity. Also, the ORR performance of such catalysts is also probed in an acidic system. Significantly, when acted as a cathode electrocatalyst for a Zn–air battery, it displays a higher power density and discharge performance than the benchmark Pt/C catalyst.

2. Experimental

2.1. Material synthesis

To obtain the precursor, banana peels (BP) were exhaustively washed with copious amount of de-ionized water, and shredded into small pieces before being dried in oven for 24 h at 80°C . The obtained precursor was then pre-carbonized under flowing Ar_2 at 300°C for 2 h, and the calcined product was grinded in a planetary ball mill for 5 h at 500 rpm. Afterward, the material was heated with the addition of KOH (BP: KOH: 1:2 wt.%) at 800°C for 1 h in Ar_2 atmosphere. The obtained product was labeled as BP-K. To remove residual KOH and unstable species from the catalyst, the sample was rinsed for one night with 0.5 M H_2SO_4 at 80°C and thoroughly washed with de-ionized water and ethanol before dried at 80°C in vacuum. Lastly, the obtained material was treated in Ar_2 at 1000°C for 105 min, followed by NH_3 treatment for 15 min. The obtained N-doped carbonized banana peel catalyst, denoted as BP-K-A where K indicates KOH activation and A indicates a NH_3 treatment. For comparison, we also prepared BP-Ar under similar conditions without KOH activation and NH_3 treatments.

2.2. Materials characterization

The morphology and structure of the samples were observed on field-emission scanning electron microscope (SEM, JSM-7100F), and high-resolution transmission electron microscopy (TEM, JEM-2100F). Micromeritics ASAP 2020 analyzer was applied to measure the Brunauer Emmett Teller (BET) surface area and pore size distribution (PSD). X-ray photoelectron spectroscopy (XPS) measurements were employed on an X-ray photoelectron spectrometer (VG-Multi-lab2000) by using Al K α radiation (1486.71 eV). Raman spectroscopy was performed on a Renishaw instrument via Ar ion laser with a 514.5 nm excitation wavelength. Inductively coupled plasma mass spectrometry (ICP-MS, ELAN DRC-e) was carried to detect the residual trace metal content of the catalysts.

2.3. Electrochemical measurements

The electrochemical measurements were carried out on a three-electrode cell (CHI660E) at room temperature. A saturated calomel electrode (SCE) and a slice of platinum were employed as reference and counter electrodes, respectively. A glassy carbon disk (5.0 mm diameter) was covered with the catalyst-ink and applied as working electrode. The ink was prepared by mixing catalyst (5.0 mg)

with Nafion solution (25 ml, 5 wt%, DuPont) and isopropyl alcohol (0.475 ml). 0.3 mg cm^{-2} catalyst was then loaded on the glassy carbon electrode. For comparison, the Pt loading was $20 \mu\text{g cm}^{-2}$. Linear sweep voltammetry (LSV) was performed by employing the rotating disk electrode (RDE) procedure in O_2 -saturated 0.1 M KOH electrolyte. Cyclic voltammetry (CV) curves were collected in a N_2 or O_2 -saturated 0.1 M KOH electrolyte with a scan rate of 20 mV s^{-1} . Additionally, the ORR activity was also evaluated via the RDE method by LSV from -0.3 to 0.7 V in O_2 -saturated 0.1 M HClO_4 electrolyte. The ORR stability in O_2 -saturated 0.1 M HClO_4 solution was tested by current versus time (i-t) test with the rotating speed of 1600 rpm. The electrochemical impedance spectroscopy (EIS) measurements were tested under open circuit potential with an excitation signal of 5 mV at frequency ranges of 100 kHz to 0.1 Hz.

For the Zn–air battery test, an air cathode was prepared by spraying the catalyst onto carbon paper, and then dried in an oven 60°C for 4 h. The catalyst mass loading was 0.8 mg cm^{-2} . A polished Zn plate was employed as the anode. These two electrodes and 6 M KOH aqueous electrolyte were assembled into a home-made Zn–air battery.

3. Results and discussion

The catalyst structure and morphology were investigated by SEM (Fig. 1a–d) and TEM (Fig. 2a–d). BP-Ar shows a typical amorphous carbon structure with segregated and non-uniform thick flakes (Fig. 1a, b). After activation by KOH and thermal treatments in NH_3 (Fig. 1c, d), BP-Ar was transformed into the graphene-like structure (BP-K-A) with the inter-connected flower-like 3D pores where transparent carbon nanosheets can be observed (Fig. 1d). For comparison, the KOH activation sample without NH_3 treatments was prepared (BP-K). As shown in Fig. S2, BP-K exhibits an identical pore morphology, demonstrating that the additional treatment in NH_3 has minimal effect on the morphology, while the KOH activation was critical for the construction of the 3D inter-connected porous carbon nanosheets (as explained below).

TEM images (Fig. 2a–c) reveal BP-K-A possesses abundant mesopores consisting of graphene-like carbon films. Fig. 2d displays the mesopores are around $\sim 2.9 \text{ nm}$ in diameter and thin films of few carbon layers interspaced $\sim 0.38 \text{ nm}$ apart. This 3D nanoscale architecture with good contact can afford continuous electron channels and benefit ion transportation because of the shortened diffusion pathway [23]. In addition, unlike traditional graphitic carbon materials, such an architecture can be efficient to prevent the stacking or aggregation of carbon nanosheets, resulting in the high surface area and porosity. Most importantly, they contain a large number of edges and defects, which are in good favour of ORR activity as previously reported [18,19,22].

N_2 adsorption-desorption isotherms were tested to analyse the porosity and specific surface area (SSA) of the prepared BP-K-A and BP-Ar samples. From the N_2 adsorption-desorption isotherms (Fig. 3a), the presence of hysteresis-loop can be classified as a type-H4 [24]. This shows the existence of mesopores, in good agreement with the TEM results. The KOH activation leads to the high SSA of BP-K-A ($1756 \text{ m}^2 \text{ g}^{-1}$), which is not only much larger than other reported biomass derived carbon materials, but also higher than previously reported graphene-based materials, such as graphene foams, aerogels, and frameworks [18,21,22,25–27]. The PSD of BP-K-A (inset of Fig. 3a) shows it possesses mesopores in the range of 2.6–2.9 nm. On the contrast, BP-Ar (Fig. S3a) has a relatively lower BET SSA ($913 \text{ m}^2 \text{ g}^{-1}$) nearly half of BP-K-A, demonstrating that the enrichment of porosity is predominantly caused by the KOH treatment. The high SSA could bring forth the exposure of more active sides, while the inter-connected mesoporous structure can enhance the ORR diffusion relevant ions [28]. These unique

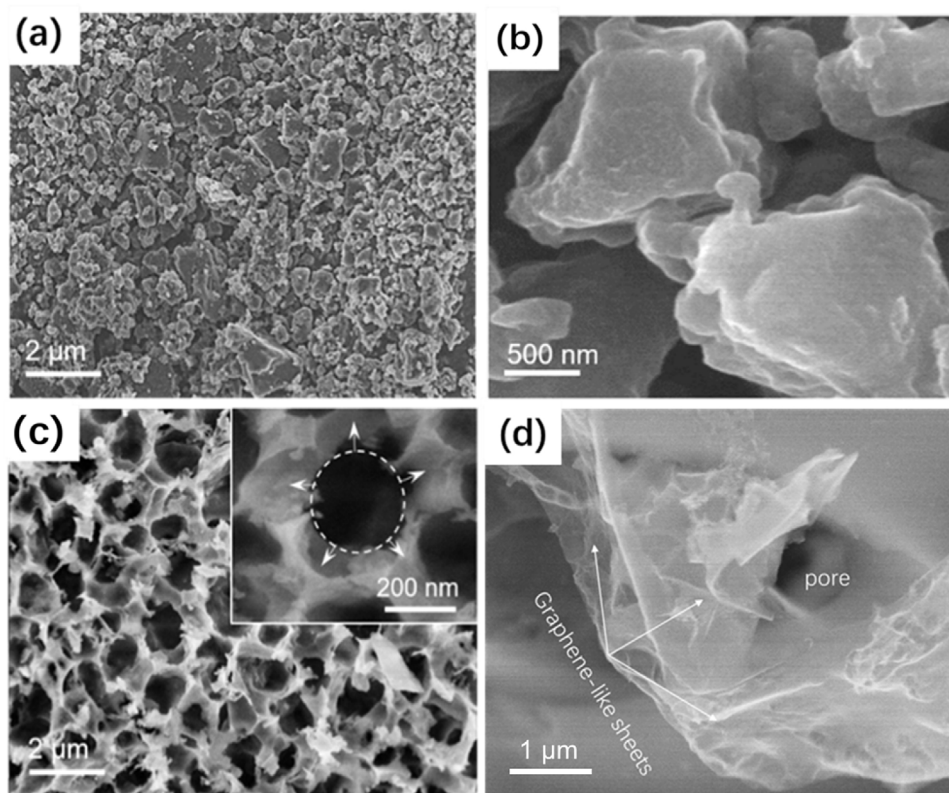


Fig. 1. SEM images of BP-Ar (a, b), BP-K-A (c, d).

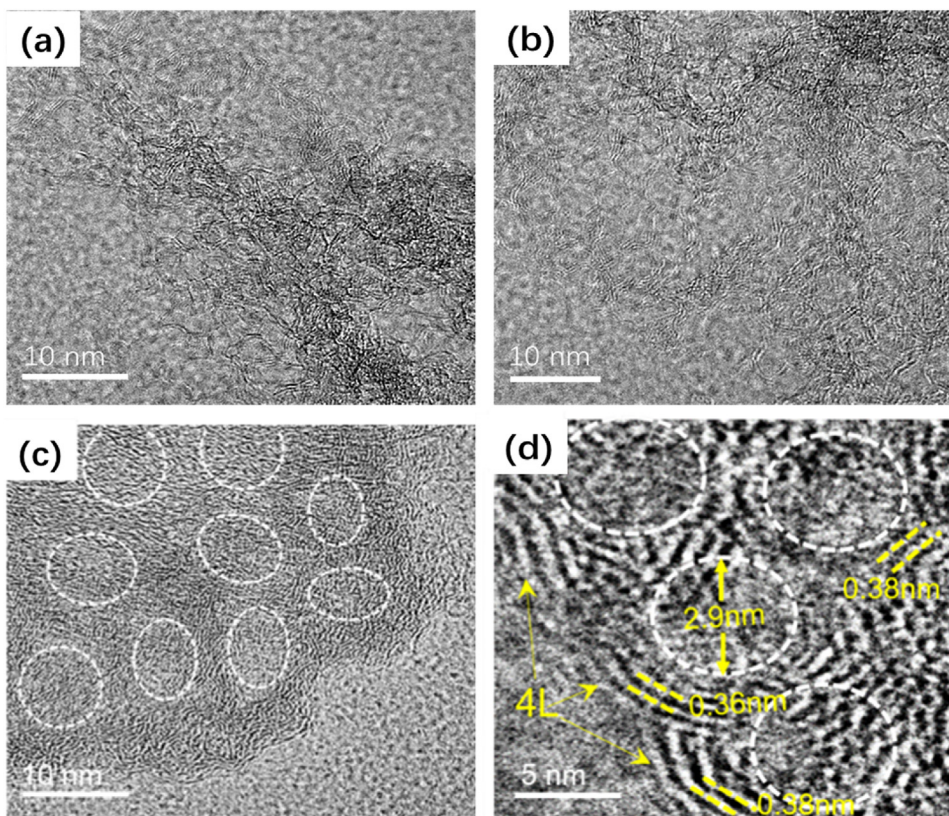


Fig. 2. TEM of BP-K-A (a–d). White cycles indicate pores.

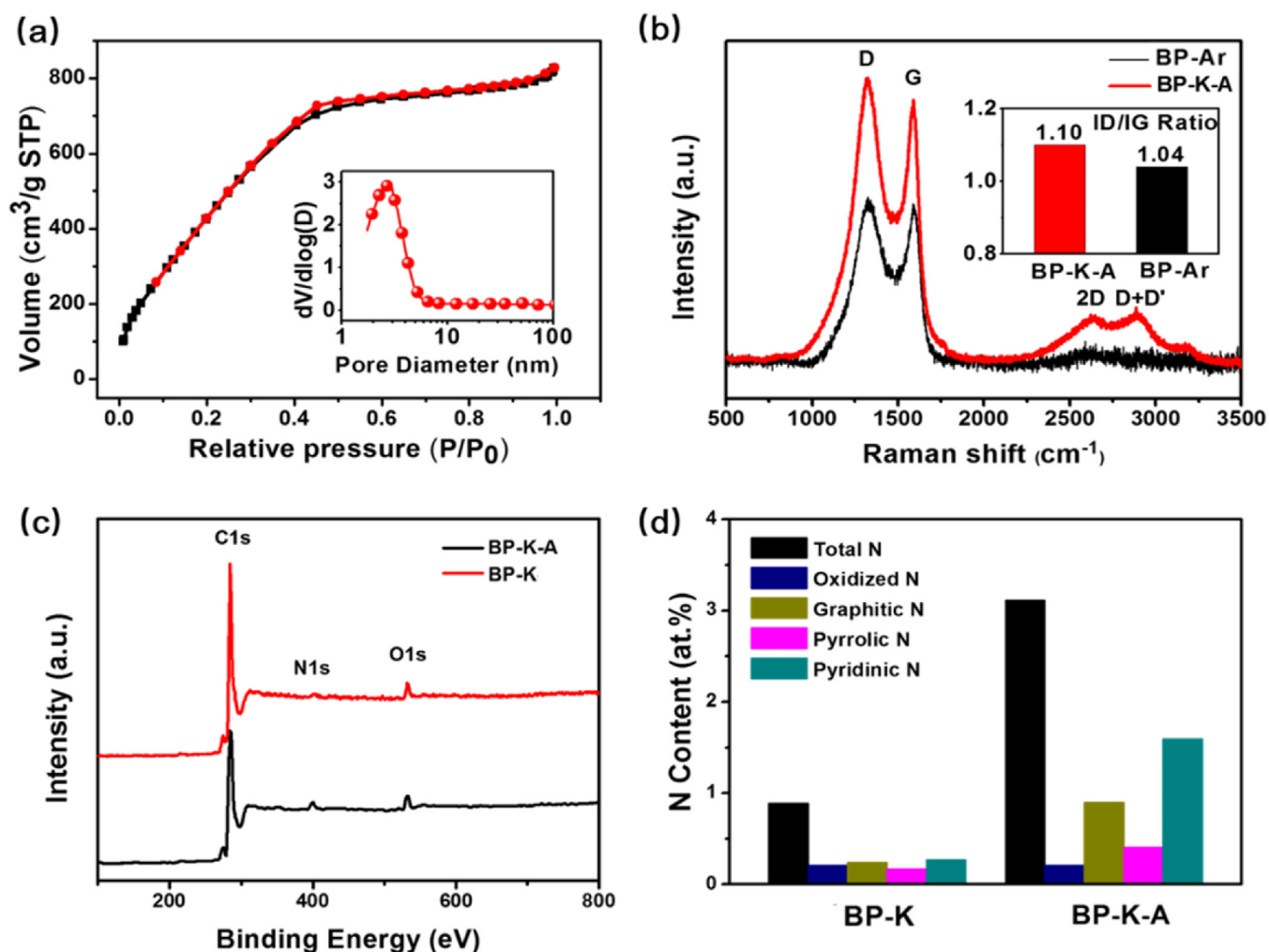


Fig. 3. (a) Nitrogen adsorption-desorption isotherm and pore size distribution (inset) of BP-K-A catalyst, (b) the Raman spectra of BP-Ar and BP-K-A, (c) XPS survey spectra of BP-K and BP-K-A, (d) the N1s fitted results of BP-K and BP-K-A extracted from Fig. S3b–c and Table S1.

features of the as-prepared material would be responsible for the significantly enhanced ORR activity.

As shown in Fig. 3b, Raman spectroscopy was employed to examine the carbon structure. BP-K-A displays four characteristic peaks within 1000–3500 cm⁻¹, including D (~1325 cm⁻¹), G (~1587 cm⁻¹), D+D' (~2875 cm⁻¹) and 2D (~2645 cm⁻¹) bands [29,30]. Among them, the D and G bands correspond to the disorder or defects induced feature in sp² carbons and the graphitic carbon, while the 2D peak (2636 cm⁻¹) is the D-peak overtone, and a minor D+D' peak appearing at around 2900 cm⁻¹ is the combination mode of D and D', resulting from a two-phonon defect-induced process [29,30]. The broader peak width at half height of D peak in BP-K-A indicates it contains a large number of edges and defects (Fig. 3b). The I_D/I_G value is often employed to estimate the degree of defects in carbon-based materials [29,30]. The higher I_D/I_G ratio of BP-K-A (1.10) than that of BP-Ar (1.03) can be ascribed to the distortion of the carbon structure and the defects induced by nitrogen doping and KOH activation, which are beneficial for enhancing the ORR activity. The 2D peak is one of the typical features of graphene in Raman spectroscopy in which its shape and position can be employed to identify the layers number of graphene-like carbon sheets approximately [10]. BP-K-A displays a clear 2D band, which supports the graphene-like carbon structure as revealed by the SEM (Fig. 1d). In comparison with the Raman spectral of monolayer graphene [31], BP-K-A owns a broader peak, demonstrating

the presence of graphene-like carbon nanosheets with few layers as exhibited by TEM (Fig. 2d).

XPS survey spectra (Fig. 3c) indicate the catalysts predominantly consist of N, C, and O elements, among which the amount of nitrogen is 3.11 at.% for BP-K-A and 0.89 at.% for BP-K, suggesting successful doping of N atoms into the carbon framework after annealing in NH₃. Fig. S3b and 3c show the deconvoluted peaks from N1s peaks of BP-K-A and BP-K, which are corresponding to oxidized N (402.3 ± 0.2 eV), graphitic N (401.1 ± 0.2 eV), pyrrolic N (400.1 ± 0.2 eV) and pyridinic N (398.2 ± 0.2 eV) species, respectively [32]. It has been established that pyridinic N in nitrogen doped carbon frameworks can bring the active sites for ORR, whereby the carbon atoms next to the pyridinic N are considered as the active sites during the ORR process [33]. BP-K-A possesses a higher content of active N (pyridinic N) than BP-K, indicating that the ORR activity would be improved. In addition, to exclude the influence of the residual trace metal in the catalyst in which BP contains various metal elements, ICP-MS was performed. As displayed in Table S2, the residual metal content is extremely low (ppm level) in both BP-K-A and BP-K, owing to the long-time repeated acid pickling, which could be considered as metal-free catalyst if the test error is considered.

On the basis of the above results, the formation mechanism of such 3D inter-connected porous architecture with graphene-like carbon nanosheets is proposed, as shown in Fig. 4. The biomass

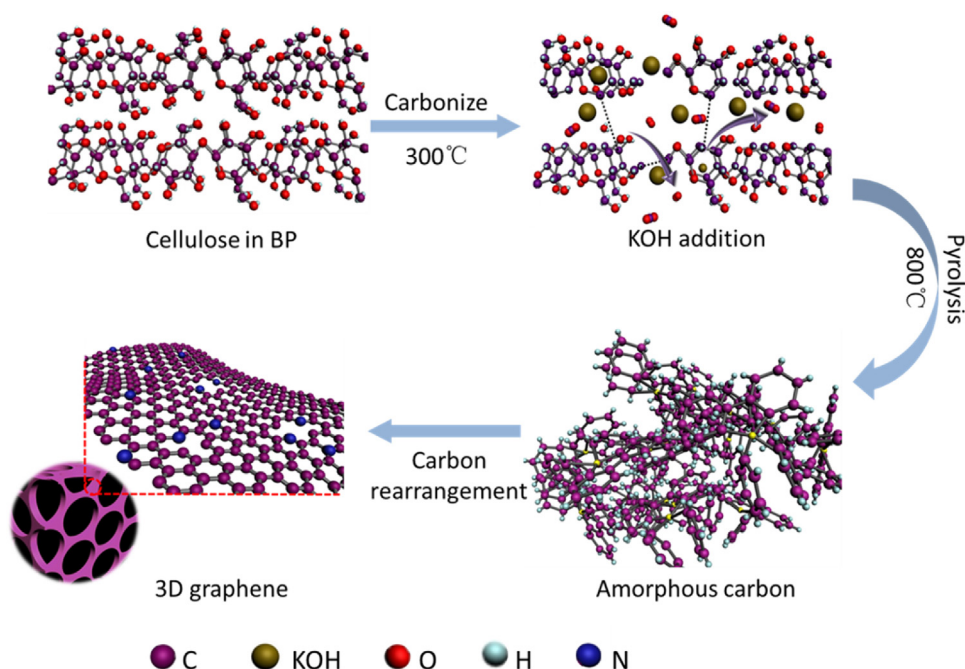
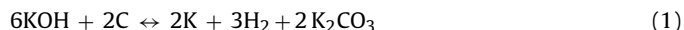


Fig. 4. Illustration of the formation mechanism of 3D carbon nanosheets.

BP is mainly composed of cellulose with intrinsic porosity (Fig. S1). After pre-carbonized, the intrinsic pore structure can be well preserved, which is beneficial for KOH insertion and reaction with carbon. The predominant stoichiometry reaction of the activation is given as [34–36]



where K_2CO_3 can be further decomposed into K_2O , CO_2 and CO . These products can further etch carbon to promote the porosity [34–37]. In this process, on one hand, the etching-out carbon units leads to the formation of porous structures with near-uniform sizes. The formation of porous network is reckoned to enhance SSA as previously observed in literature [38,39]. On the other hand, metallic potassium (K) acts as an in-situ generated catalyst to promote the formation of graphitic carbon which subsequently self-organized into the graphene-like structure. Moreover, the hexatomic ring chains of the cellulose in BP predominantly composed of carbon and oxygen atoms could also benefit the construction of the graphene-like carbon sheet structures under the given conditions without adding any metal catalysts.

To evaluate the electrocatalytic activity of the as-prepared catalysts, CV and LSV were measured. As shown in Fig. 5a, the BP-K-A displays a clearly distinct oxygen reduction peak at -0.162 V , which is positive than that of commercial Pt/C (-0.17 V). As observed, BP-K-A also displays a higher oxygen reduction peak potential than BP-K (-0.25 V), indicating the higher electrocatalytic activity for ORR in BP-K-A caused by the nitrogen doping. Two important parameters, half-wave potential ($E_{1/2}$) and onset potential (E_0), were adopted to compare the ORR activities of the catalysts (from LSV measurements, Fig. 5b), where $E_{1/2}$ and E_0 of all the catalysts were taken according to the potential at which the reduction current density is 50% and 5%, respectively [40,41]. The ORR activity of the BP-K ($E_0 = -0.085\text{ V}$, $E_{1/2} = -0.28\text{ V}$) is much inferior to Pt/C ($E_0 = -0.05\text{ V}$, $E_{1/2} = -0.2\text{ V}$) (Fig. 5b). However, after annealing in NH_3 atmosphere, the ORR activity of as prepared BP-K-A ($E_0 = -0.03\text{ V}$, $E_{1/2} = -0.17\text{ V}$) is significantly improved and even better than that of Pt/C. While for BP-Ar (without KOH activation and NH_3 treatment), its ORR activity is relatively very poor (Fig. S4),

indicating both of KOH activation and NH_3 treatments are promisingly important to boost the ORR activity. So far as we know, such high ORR activity of BP-K-A is higher than other reported biomass derived carbon catalysts [17,18,22,41], as well as some graphene-based catalysts, including graphene foams, nanoribbons, and aerogels frameworks [15,25–27].

To gain further understanding of the ORR mechanism, the reaction kinetics was evaluated via the ORR polarization for BP-K-A and BP-K at different rotation rates from 400 to 2000 rpm, as shown in Fig. 5c and d, respectively. According to the data, the Koutecky-Levich (K-L, Supporting Information) curves at the different potentials exhibit a good linearity (inset of Fig. 5c, d). The calculated average electron transfer number (n) for is 3.1 and 3.95 for BP-K and BP-K-A, respectively, which is approximately equivalent to the theoretical transfer route of four electrons for Pt-based catalysts. Fig. 5e shows Nyquist plots of catalysts, where the intersection with the x-axis at the high frequency represents the solution resistance, the semicircle part between the high frequency and low frequency domains is the charge transfer resistance, a declining line in the low frequency regions is related to the diffusion-controlled process. [14] Bode plots of all the catalysts (Fig. S5) suggest a one-time constant process in alkaline media. In accordance with the equivalent circuit (Fig. S6), the fitted results present that the charge transfer resistance of BP-K-A ($9.3\ \Omega\text{ cm}^{-2}$) is significantly lower than BP-K ($13.5\ \Omega\text{ cm}^{-2}$) and close to that of Pt/C ($8.4\ \Omega\text{ cm}^{-2}$), implying a high charge transfer rate in BP-K-A, which is in favour of improvement of ORR activity. Meanwhile, the Tafel slope (Fig. 5f) of BP-K-A (63 mV decade^{-1}) is much lower than that of BP-K (85 mV decade^{-1}) and very approach to that of Pt/C (65 mV decade^{-1}), demonstrating that the ORR mechanism of BP-K-A is similar to Pt/C in an alkaline electrolyte [39]. The outstanding ORR activity of BP-K-A can be mainly ascribed its laminated graphene-like structure and unique nature: the ultra-high surface area can expose additional active sites to increase the catalytic activity; the excellent porous structure can efficiently facilitate the diffusion of ORR ionic species; the rich edge defects and the good electrical conductivity of graphene-like carbon can further enhance the ORR activity. Meanwhile, the high active nitro-

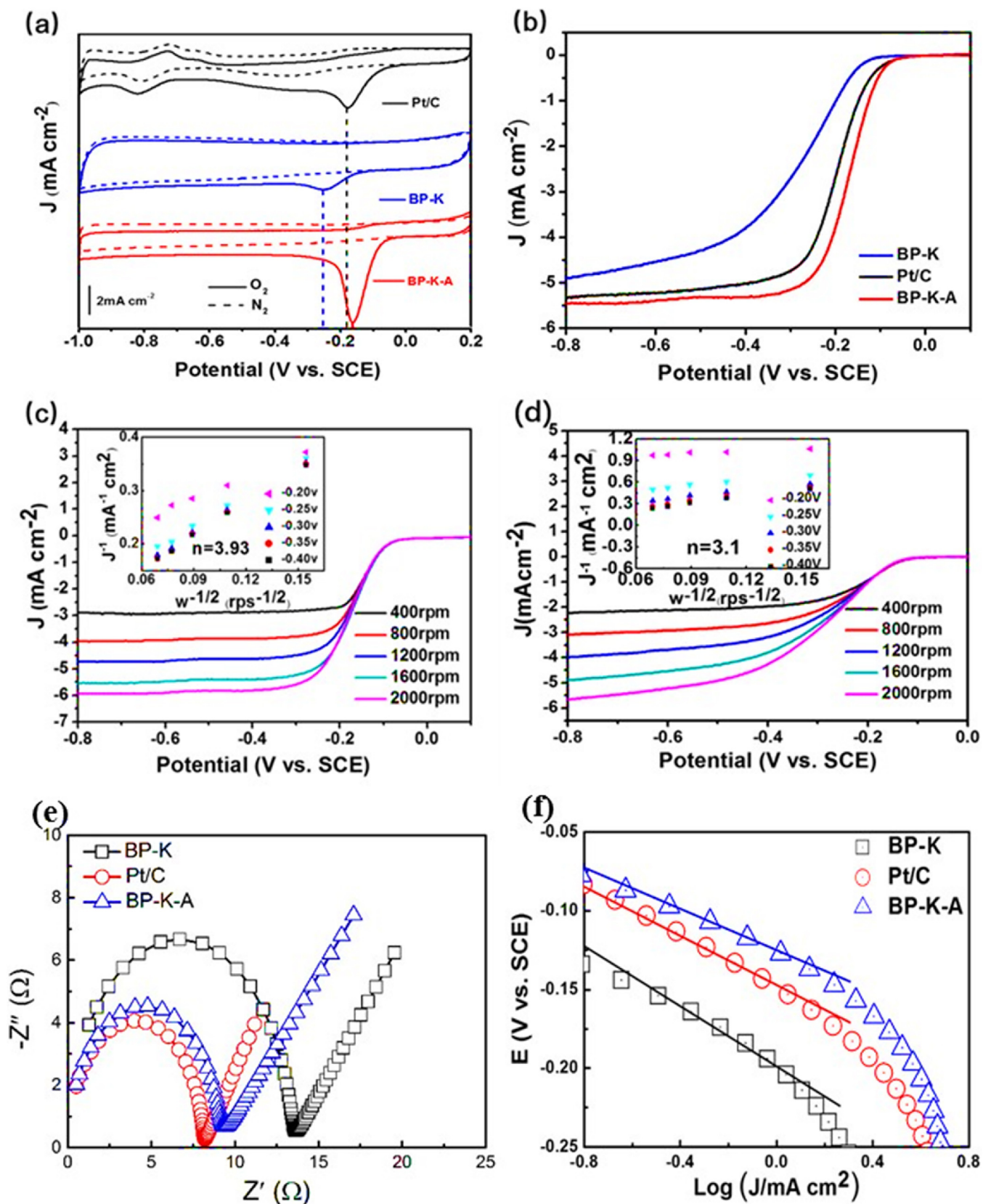


Fig. 5. CV (a) and LSV (b) curves of Pt/C, BP-K-A, and BP-K, (c) LSV curves of BP-K-A at different rotation rates, inset: the corresponding K-L plots of BP-K-A; (d) LSV curves of BP-K at different rotation rates, inset: the corresponding K-L plots of BP-K; (e) Nyquist plots of electrochemical impedance spectroscopy for BP-K-A, BP-K and Pt/C; (f) Tafel plots for BP-K-A, BP-K and Pt/C extracted from Fig. 5b. Data was recorded in 0.1 M KOH solution. Dash lines are a guide to eye.

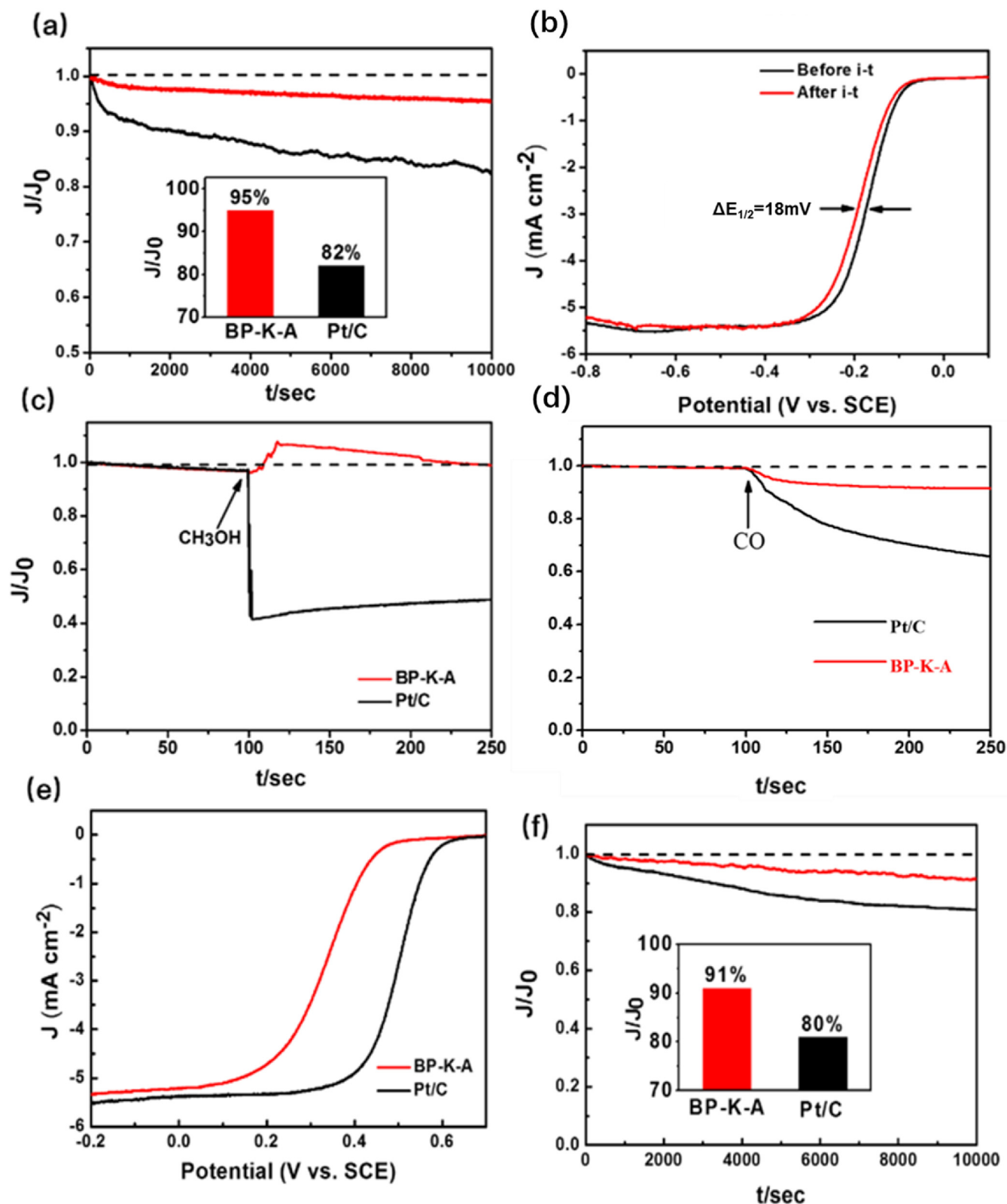


Fig. 6. (a) The current vs. time (i-t) chronoamperometric responses of BP-K-A and Pt/C durability, inset: the ratio of the J/J_0 , (b) the stability of BP-K-A is symbolized by $\Delta E_{1/2}$ before and after i-t test, (c) Methanol tolerance (1 M), and (d) CO tolerance ($V_{\text{CO}}/V_{\text{O}_2} \approx 10\%$). Data (a–d) was recorded in 0.1 M KOH solution in O_2 -saturated during a constant potential at -0.35 V and a rotation rate of 1600 rpm. (e) LSV curves of BP-K-A and Pt/C in 0.1 M HClO_4 solution, (f) the i-t chronoamperometric responses of BP-K-A and Pt/C at 0.3 V with a rotation speed of 1600 rpm in O_2 -saturated 0.1 M HClO_4 solution, inset: the ratio of the J/J_0 . Dash lines are a guide to eye.

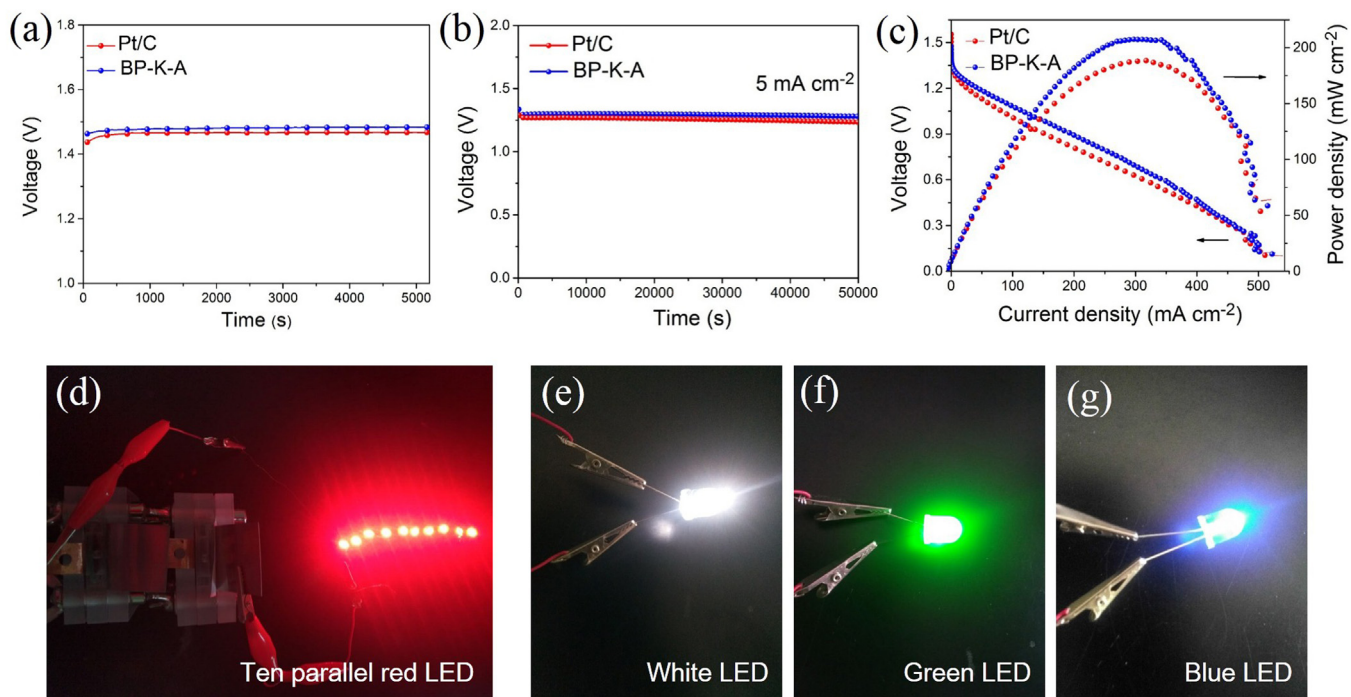


Fig. 7. (a) Open circuit voltage measurements and (b) polarization curves and power density plots and (c) discharge curves of Zn-air batteries fabricated with BP-K-A and Pt/C catalysts. Photographs of (d) ten parallel red and high voltage of (e) white, (f) green and (g) blue LED lamp beads driven by two Zn-air batteries with the BP-K-A electrode connected in series. (For interpretation of the references to colour in this figure legend, the reader is referred to the web version of this article.)

gen doped content leads to a remarkable ORR activity for BP-K-A in alkaline media.

The *i*-*t* chronoamperometric response was examined to compare the stability of BP-K-A catalysts with that of Pt/C. BP-K-A displayed 95% relative current retention after 10000 s, indicating a better stability than Pt/C (82%) (Fig. 6a). On the other hand, the decay of half-wave potential ($\Delta E_{1/2}$, before and after *i*-*t* measurements) of Pt/C is 32 mV (Fig. S7), which is much higher than that of BP-K-A ($\Delta E_{1/2} = 18$ mV) as displayed in Fig. 6b. These results also prove that our catalyst is electrochemically extremely durable than Pt/C in the alkaline electrolyte. The outstanding durability can be assigned to the stabilized graphene-like structure of BP-K-A while Pt nanoparticle migration and aggregation occur within carbon supported Pt catalysts [5,42]. Interestingly, BP-K-A also exhibits excellent resistance against CO poisoning as well as methanol crossover. As shown in Fig. 6c, after the injection of 3 M methanol, the BP-K-A catalyst shows only slight change of relative ORR currents. In contrast, Pt/C loses over 51% of the initial relative current within 150 s. Similarly, after injecting CO into the O₂-saturated 0.1 M KOH solution, the relative current density of Pt/C is quickly dropped (35% within ~150 s), whereas BP-K-A is almost insensitive to CO poisoning (Fig. 6d). These results reveal our catalyst owns superior durability and immunity to CO poisoning and methanol crossover compared with Pt/C, signifying a promising cathode catalyst for alkaline fuel cells.

Furthermore, we explored the ORR performance of BP-K-A in acidic media. As shown in Fig. 6e, BP-K-A exhibits good ORR activity in acidic electrolyte as well. Although the $E_{1/2}$ of BP-K-A (0.33 V) is 160 mV lower than Pt/C (0.49 V), it is favourably comparable to recently reported heteroatom-doped carbon based catalysts in acid electrolytes [43–45]. The *i*-*t* test result shows a relative current preservation rate of 91% for BP-K-A after 10000 s test, which is also superior compared to that of Pt/C (81%) in the same range (Fig. 6f). These above mentioned results demonstrate that the BP-K-A catalyst also possesses an excellent electrochemical durability in an acidic medium.

Considering the excellent ORR performance of BP-K-A, a home-made Zn-air battery device was fabricated with zinc plate as an anode and BP-K-A loaded on carbon cloth as an air cathode. For comparison, the commercial Pt/C catalyst was also tested under the same conditions. As shown in Fig. 7a, the assembled Zn-air battery using BP-K-A as the air cathode displays a higher open-circuit voltage than that of Pt/C electrode. Fig. 7b shows the discharge polarization and power density curves of zinc-air batteries. It is revealed that the BP-K-A cathode has the higher peak power density of 208 mW cm⁻² than Pt/C electrode (189 mW cm⁻²) due to the excellent ORR activity of BP-K-A. The galvanostatic discharge curves (Fig. 7c) also exhibit that the BP-K-A cathode owns a high voltage plateau of 1.31 V at the discharge current density of 5 mA cm⁻², which exceeds that of the Pt/C electrode (1.27 V at 5 mA cm⁻²). This is mainly attributed to its open 3D hierarchical porous architectures with high surface area, supplying a fast electronic transport channel and accessible mass transfer in the reaction boundary for oxygen reduction. When two Zn-air batteries were connected in series, as exhibited in Fig. 7d, they can drive ten parallel high-power red light-emitting diode (LED) lamp beads and keep it bright for a long time. Additionally, as shown in Fig. 7e–f, they can also power high voltage LED lamp beads (white, green and blue, 3.0–3.2 V). These results further demonstrate that such 3D N-doped carbon nanosheet catalyst can be a good alternative to the precious Pt catalyst for ORR in practical applications.

4. Conclusion

Unique N-doped 3D carbon nanosheets with high specific surface (1756 m² g⁻¹) are synthesized using waste biomass only by facile heat treatments and potassium hydroxide activation. To further adjust nitrogen amount and types, nitrogen doping is performed, the nitrogen-doped 3D carbon possessing higher nitrogen content exhibits outstanding electrochemical ORR activity in an alkaline medium in comparison with commercial Pt/C, and evidently demonstrates superior tolerance and stability in both

alkaline and acidic systems. The high activity can be assigned to the unique 3D carbon nanosheet structure which possesses reasonable pore size distribution and high specific surface area, high graphitization degree, rich edge defects, and increased active doped-nitrogen content. When evaluated as the air cathode catalyst in the Zn-air battery, the as-prepared catalyst exhibits higher performance than that of the precious metal Pt catalyst. This study opens a new approach to synthesize metal-free catalysts at low-cost with superior catalytic activity toward ORR.

Acknowledgements

This work was financially sponsored by the National Natural Science Foundation of China (51372186, 516722040) and State Key Laboratory of Advanced Technology for Materials Synthesis and Processing (Wuhan University of Technology) (2017-KF-14).

Appendix A. Supplementary data

Supplementary data associated with this article can be found, in the online version, at <http://dx.doi.org/10.1016/j.apcatb.2017.04.038>.

References

- [1] M. Winter, R.J. Brodd, *Chem. Rev.* 105 (2005) 1021.
- [2] B.C.H. Steele, A. Heinzel, *Nature* 414 (2001) 345–352.
- [3] M.K. Debe, *Nature* 486 (2012) 43–51.
- [4] V.R. Stamenkovic, B. Fowler, B.S. Mun, G. Wang, P.N. Ross, C.A. Lucas, N.M. Marković, *Science* 315 (2007) 493–497.
- [5] D. He, S. Mu, M. Pan, *Carbon* 49 (2011) 82–88.
- [6] D. Yang, D. Bhattacharjya, S. Inamdar, S. Inamdar, J. Ark, J. Yu, *J. Am. Chem. Soc.* 134 (2012) 16127–16130.
- [7] L. Yang, S. Jiang, Y. Zhao, L. Zhu, S. Chen, X. Wang, Q. Wu, J. Ma, Y. Ma, Z. Hu, *Angew. Chem.* 123 (2011) 7270–7273.
- [8] S. Inamdar, H. Choi, P. Wang, M. Song, J. Yu, *Electrochem. Commun.* 30 (2013) 9–12.
- [9] K. Gong, F. Du, Z. Xia, M. Durstock, L. Dai, *Science* 323 (2009) 760–764.
- [10] D. Geng, Y. Chen, Y. Chen, Y. Li, R. Li, X. Sun, S. Ye, S. Knights, *Energy Environ. Sci.* 4 (2011) 760–764.
- [11] R. Liu, D. Wu, X. Feng, K. Müllen, *Angew. Chem.* 122 (2010) 2619–2623.
- [12] X. Zhou, Z. Yang, H. Nie, Z. Yao, L. Zhang, S. Huang, *J. Power Sources* 196 (2011) 9970–9974.
- [13] S. Chen, J. Bi, Y. Zhao, L. Yang, C. Zhang, Y. Ma, Q. Wu, X. Wang, Z. Hu, *Adv. Mater.* 2 (2012) 424.
- [14] J. Biener, M. Stadermann, M. Suss, M.A. Worsley, M.M. Biener, K.A. Rose, T.F. Baumann, *Energy Environ. Sci.* 4 (2011) 656–667.
- [15] V. Chabot, D. Higgins, A. Yu, X. Xiao, Z. Chen, J. Zhang, *Energy Environ. Sci.* 7 (2014) 1564–1596.
- [16] Z. Wu, H. Liang, L. Chen, B. Hu, S. Yu, *Acc. Chem. Res.* 49 (2016) 96–105.
- [17] P. Hao, Z. Zhao, Y. Leng, J. Tian, Y. Sang, R.I. Boughton, C.P. Wong, H. Liu, B. Yang, *Nano Energy* 15 (2015) 9–23.
- [18] X. Wang, Y. Zhang, C. Zhi, X. Wang, D. Tang, Y. Xu, Q. Weng, X. Jiang, M. Mitome, D. Golberg, Y. Bando, *Nat. Commun.* 4 (2013) 2905.
- [19] Z. Wu, Y. Sun, Y. Tan, S. Yang, X. Feng, K. Müllen, *J. Am. Chem. Soc.* 134 (2012) 19532–19535.
- [20] Fairtrade International, <http://www.fairtrade.net/products/bananas.html>. 2016–7–19.
- [21] M.M. Titirici, R.J. White, C. Falco, M. Sevilla, *Energy Environ. Sci.* 5 (2012) 6796–6822.
- [22] H. Zhou, J. Zhang, I.S. Amiinu, C. Zhang, X. Liu, W. Tu, M. Pan, S.C. Mu, *Phys. Chem. Chem. Phys.* 18 (2016) 10392–10399.
- [23] Z. Li, L. Zhang, B.S. Amirkhiz, X. Tan, Z. Xu, H. Wang, B.C. Olsen, C.M.B. Holt, D. Mitlin, *Adv. Energy Mater.* 2 (2012) 431–437.
- [24] Y. Li, H. Zhang, P. Liu, Y. Wang, H. Yang, Y. Li, H. Zhao, *Electrochem. Commun.* 51 (2015) 6–10.
- [25] Z. Wu, S. Yang, Y. Sun, K. Parvez, X. Feng, K. Müllen, *J. Am. Chem. Soc.* 134 (2012) 9082–9085.
- [26] Y. Xue, D. Yu, L. Dai, R. Wang, D. Li, A. Roy, F. Lum, H. Chen, Y. Liu, J. Qu, *Phys. Chem. Chem. Phys.* 15 (2013) 12220–12226.
- [27] Y. Zhao, C. Hu, Y. Hu, H. Cheng, G. Shi, L. Qu, *Angew. Chem.* 124 (2012) 11533–11537.
- [28] H. Liang, W. Wei, Z. Wu, X. Feng, K. Müllen, *J. Am. Chem. Soc.* 135 (2013) 16002–16005.
- [29] C. Andrea, M. Denis, *Nat. Nanotechnol.* 8 (2013) 235–246.
- [30] D. Elias, R. Nair, T. Mohiuddin, S. Morozov, P. Blake, M. Halsall, A. Ferrari, D. Boukhvalov, M. Katsnelson, A. Geim, *Science* 323 (2009) 610–613.
- [31] C. Lui, L. Liu, K.F. Mak, G.W. Flynn, T.F. Heinz, *Nature* 462 (2009) 339–341.
- [32] J. Zhang, D. He, H. Su, X. Chen, M. Pan, S. Mu, *J. Mater. Chem. A* 2 (2014) 1242–1246.
- [33] D. Guo, R. Shibuya, C. Akiba, S. Saji, T. Kondo, J. Nakamura, *Science* 351 (2016) 361–365.
- [34] J. Wang, S. Kaskel, *J. Mater. Chem.* 22 (2012) 23710–23725.
- [35] Y.F. Zhao, W. Ran, J. He, Y.F. Song, C.M. Zhang, D.B. Xiong, F.M. Gao, J.S. Wu, Y.Y. Xia, *ACS: Appl. Mater. Interfaces* 7 (2015) 1132–1139.
- [36] Z. Zhang, S.C. Mu, B.W. Zhang, L. Tao, S.F. Huang, Y.Z. Huang, F.M. Gao, Y.Y. Zhao, *J. Mater. Chem. A* 4 (2016) 2137–2146.
- [37] D. Lozano-Castello, M.A. Lillo-Rodenas, D. Cazorla-Amorós, A. Linares-Solano, *Carbon* 39 (2001) 741–749.
- [38] D. Lozano-Castello, J.M. Calo, D. Cazorla-Amorós, A. Linares-Solano, *Carbon* 45 (2007) 2529–2536.
- [39] E. Raymundo-Piñero, P. Azaïs, T. Cacciaguerra, D. Cazorla-Amorós, A. Linares-Solano, F. Béguin, *Carbon* 43 (2005) 786–795.
- [40] J. Liu, X. Sun, P. Song, Y. Zhang, W. Xing, W. Xu, *Adv. Mater.* 25 (2013) 6879–6883.
- [41] J. Zhang, S. Wu, X. Chen, K. Cheng, M. Pan, S. Mu, *RSC Adv.* 4 (2014) 32811–32816.
- [42] H.F. Lv, S.C. Mu, *Nanoscale* 6 (2014) 5063–5074.
- [43] M.H. Robson, A. Serov, *Electrochim. Acta* 90 (2013) 656–665.
- [44] Y. Zhu, B. Zhang, X. Liu, D. Wang, D. Su, *Angew. Chem.* 53 (2014) 10673–10677.
- [45] B. Merzouguia, A. Hachimia, A. Akinpelua, S. Bukolaa, M. Shao, *Electrochim. Acta* 107 (2013) 126–132.